



Surface Morphology and Structural Evolution of Magnetite-Based Iron Ore Fines During the Oxidation

HENG ZHENG, JOHANNES SCHENK, RUNSHENG XU, ODAY DAGHAGHELEH, DANIEL SPREITZER, THOMAS WOLFINGER, DAIWEI YANG, and YURY KAPELYUSHIN

The use of magnetite-based iron ore fines by means of fluidized bed technology has become a promising route to produce direct reduced iron. The significant influence of a prior oxidation treatment, which occurs in the preheating stage, on the subsequent fluidization and reduction behavior was observed in our previous study. As a result, it is important to investigate the oxidation of magnetite-based iron ore fines for an optimization of the proposed route. Three magnetite-based iron ore brands were analyzed. The oxidation characteristics are investigated based on thermogravimetric analysis. The surface morphology, structural evolution, and phase transformation were studied with a scanning electron microscope, an optical light microscope, and a high-temperature-X-ray diffraction (HT-XRD), respectively. The three samples showed different oxidation capacity indexes (OCIs) but similar TG-DTG curves. The oxidation rate peaks at around 330 °C and 550 °C indicated the formation of γ -Fe₂O₃ and α -Fe₂O₃. The hematite phase shows a particular growth habit. The oxidation first occurs at the surface, forming gridlike hematite structures, and then extends to the inside, resulting in hematite needles. The specific surface area and pore volume decrease significantly due to the sintering effect during oxidation.

<https://doi.org/10.1007/s11663-022-02475-9>

© The Author(s) 2022

I. INTRODUCTION

OVER the past few decades, the ironmaking industry has consumed a great deal of high-grade hematite-based iron ores, which were used as iron carriers in the blast furnace process. Natural magnetite is widely present in

various rock minerals.^[1] In 2015, the world production of magnetite-based iron ore was approximately 583 million tons, which accounts for 28 pct of the total iron ore production.^[2] Generally, the magnetite-based iron ore is ground to a small particle size to release magnetite minerals from its rock matrix, followed by a magnetic separation (or flotation) to increase the iron content.^[1,3] The current practice of ironmaking from magnetite-based iron ore involves a pelletization^[4] or sintering process^[5] to obtain an appropriate size range before charging in the ironmaking facilities, such as a blast furnace,^[6–8] grate-rotary kiln,^[9] and Midrex shaft furnace.^[10,11] Nowadays, reducing CO₂ emissions is one of the most critical issues. To reach the goal of climate neutrality (net-zero greenhouse gas emissions) by 2050, new ironmaking and steelmaking technologies and concepts are required for further decreasing the overall CO₂ emissions.^[12,13]

Compared with the traditional blast furnace-basic oxygen furnace (BF-BOF) integrated route, the natural gas-based direct reduction–electric arc furnace route provides a 40 to 60 pct reduction in CO₂ emissions, from 1.6 to 2.2 tons CO₂ emission to 0.6 to 1.15 tons CO₂ emission per ton of crude steel.^[14] One possible concept for future crude steel production is using the hydrogen-gas-based fluidized bed technology to produce

HENG ZHENG and ODAY DAGHAGHELEH are with the Chair of Ferrous Metallurgy, Montanuniversitaet Leoben, Franz-Josef-Straße 18, 8700 Leoben, Austria. Contact e-mail: heng.zheng@stud.unileoben.ac.at JOHANNES SCHENK is with the Chair of Ferrous Metallurgy, Montanuniversitaet Leoben and also with the K1-MET GmbH, Stahlstraße 14, 4020, Linz Austria. RUNSHENG XU is with the The State Key Laboratory of Advanced Metallurgy, University of Science and Technology Beijing, Beijing 100083, China. DANIEL SPREITZER is with the Primetals Technologies Austria GmbH, Turmstraße 44, 4020 Linz, Austria. THOMAS WOLFINGER is with the K1-MET GmbH. DAIWEI YANG is with the The State Key Laboratory of Refractories and Metallurgy, Wuhan University of Science and Technology, Wuhan 430081, China. YURY KAPELYUSHIN is with the South Ural State University (National Research University), Lenina Avenue 76, Chelyabinsk, Russian Federation, 454080.

Manuscript submitted October 17, 2021; accepted February 13, 2022.

Article published online March 23, 2022.

carbon-free direct reduced iron (DRI), followed by use of an electric arc furnace.^[15,16] Compared to current BF-BOF production, when the process is operated with 55 pct green hydrogen together with 45 pct natural gas, theoretically, 82 pct CO₂ emission can be avoided. When 100 pct green hydrogen is used, CO₂ emission can be reduced by more than 95 pct.^[17] Therefore, the production of DRI using magnetite-based iron ores in a hydrogen-induced fluidized bed becomes of great interest. In our previous study, direct use of magnetite-based iron ore for hydrogen-induced fluidized bed reduction was introduced.^[18,19] A series of laboratory-scale experiments were carried out to test the potential industrial application. The proposed route involves a prior oxidation treatment occurring in the preheating stage, which could improve both fluidization and reduction behavior. Compared with the deep oxidation treatment, partial oxidation of the magnetite-based iron ore was more beneficial during the final reduction stage.^[18,19] As a result, it is important to investigate the oxidation of magnetite-based iron ore for an optimization of the proposed route. However, most of the research about oxidation of magnetite-based iron ores was conducted in briquettes or pellets and mainly discussed the thermal volume change, porosity evolution, and oxidation kinetics.^[20–27] Limited literature is available for oxidation of magnetite-based iron ore in particle scale.

Colombo *et al.*^[28,29] and Basta^[30] used differential thermal analysis (DTA) and X-ray diffraction (XRD) measurements to test the oxidation of natural magnetite particles and found that the oxidation was a two-stage process: surface oxidation and further inside oxidation. In the first stage, the oxidation of Fe²⁺ to Fe³⁺ caused the diffusion of iron ions from inside the crystals of the Fe₃O₄ toward the surface. An intermediate-phase solid solution of γ -Fe₂O₃ in Fe₃O₄ was formed at the beginning of the oxidation. Then, the stable α -Fe₂O₃ (hematite) phase appeared at the surface of the magnetite particle. In the following stage, the intermediate phase transformed into α -Fe₂O₃ and completed the oxidation of the individual particle. Hyeon *et al.*^[31,32] investigated the oxidation of magnetite concentrates, which were assumed to follow a Rosin–Rammler size distribution. The oxidation behavior of the magnetite pellet was then predicted based on the oxidation kinetics of the magnetite concentrates. Apart from the oxidation kinetic analysis of magnetite particles,^[24,33–35] Song and Pistorius^[36] observed the hematite whiskers during the oxidation of magnetite concentrates. The whiskers formed in the early oxidation process and did not grow during the further oxidation. The formation of hematite whiskers was explained by a volume increase during the

structure change from magnetite to hematite, which may cause a considerable compressive stress. The formation of hematite helped to relieve the compressive stress and make the structure stable.

Zheng *et al.*^[37] summarized the oxidation behaviors and kinetics of magnetite in particle scale. Theoretically, after oxidation from magnetite to hematite, the volume will increase around 2.5^[38] to 5.2 pct.^[39] In fact, during the oxidation of magnetite-based iron ore fines, the sintering effect cannot be ignored. The specific surface area usually decreases greatly after oxidation.^[40,41] The sintering effect also shows a negative influence on the reduction of iron ore particles. The purpose of this study is to investigate the oxidation behavior of the magnetite-based iron ore fines and characterize the pores, morphology, and internal structure after oxidation. The *in-situ* high-temperature–X-ray diffraction (HT-XRD) was used to investigate the phase transformation during the oxidation process.

II. EXPERIMENTAL

A. Materials

Three commercial magnetite-based iron ore fines were used in this study. The main chemical analyses of samples A through C are listed in Table I. The particle size distributions and apparent particle densities of the samples were characterized by a CILAS 1064 particle size analyzer and Ultracycrometer 1000 density analyzer, respectively. The results are listed in Table II. The raw samples were dried at 110 °C for 6 hours before all the following tests.

B. Experimental Procedures

The oxidation behavior analysis was conducted by thermogravimetric analysis (TGA). The TGA tests were conducted using an STA 409 PG thermal analyzer. For a typical test, 50 mg of the sample was heated in an Al₂O₃ crucible (5 × 8 mm o.d.) to 1100 °C under air

Table II. Particle Size Distributions and Density of the Raw Magnetite Samples

Sample	D10 (μm)	D50 (μm)	D90 (μm)	Density (g/cm ³)
A	4.84	31.16	72.94	4.95
B	4.81	28.35	62.66	4.94
C	6.10	32.25	70.16	5.09

Table I. Chemical Analysis of the Raw Magnetite Samples (Weight Percent)

Sample	Fe _{tot}	FeO	SiO ₂	Al ₂ O ₃	MgO	CaO	TiO ₂	P	S
A	67.03	25.70	2.33	0.69	0.56	0.93	0.039	<0.001	0.13
B	68.78	27.71	5.60	0.18	0.17	0.17	—	0.017	0.05
C	65.65	27.66	3.33	1.16	1.62	1.62	0.22	0.017	0.1

flow (100 mL/min) at a heating rate of 7.5 °C/min. Each test was carried out twice and showed good reproducibility.

The isothermal oxidation was performed under a laboratory air atmosphere in a muffle furnace. To minimize the sintering effect, the oxidation temperature was set as 700 °C. One gram of the sample was placed in a 60 × 10 × 7 mm magnesia boat. Based on the bulk density of the sample, the thickness of the material layer in the boat was supposed to be around 0.35 mm. The oxidation process was assumed to proceed evenly within the material layer. Four boats of samples were oxidized for a specific controlled time in a typical isothermal oxidation test. After holding for a certain period, the boats were rapidly removed from the furnace and quenched in the open air.

The HT-XRD analyses were run on a Rigaku Ultima IV XRD diffractometer using Cu as the X-ray source, with a step size of 0.02 deg and scanning time per step of 0.15 seconds. To conduct high-temperature measurements, the samples were placed on a platinum heating strip in the HTK-16 high-temperature chamber (Anton Paar). To avoid the influences of sample area and position on the XRD patterns, each HT-XRD measurement followed the same procedure: 0.3 g of raw sample was put on the heating strip and heated in vacuum to 400 °C, 600 °C, 800 °C, and 1000 °C, respectively, at a heating rate of 100 °C/min. The positions and areas of all samples should be the same. Figure 1 shows the HT-XRD measurement profile. The raw and the final oxidized samples were measured at room temperature in the scanning angle range between 25 and 65 deg. At the target temperature, one XRD measurement was conducted before changing the vacuum to the air

atmosphere. After that, the XRD measurements were conducted every 10 minutes in the scanning angle range between 32 and 41 deg.

C. Analysis and Characterization

The weight gain measured during the TGA test can be converted into the oxidation degree (w). The w is defined as shown in Eq. [1]^[42,43]:

$$w = \frac{\Delta m}{\Delta m_{theory}} \cdot 100 \text{ pct}, \quad [1]$$

where Δm and Δm_{theory} are the measured weight gain and the theoretical weight gain during the oxidation, respectively. Δm_{theory} is calculated based on the FeO content from the chemical analysis of each magnetite-based iron ore. It should be noted that the loss on ignition of the samples was ignored.

The morphology and internal structure of the samples were observed using a scanning electron microscope (SEM, Quanta 200Mk2, FEI) and an optical light microscope (Nikon MM 40 measuring microscope system, Japan), respectively. The HT-XRD patterns were identified using Jade 6.0 software. There was a minor shift in HT-XRD peaks due to the thermal expansion of the samples, which was taken into consideration while identifying the peaks. This shift phenomenon also appeared in the HT-XRD analysis of oxidation of pyrite.^[44]

The pore structure was evaluated by the N₂ gas adsorption method using a TriStar 3000 surface area analyzer. All the samples were degassed at 200 °C for 2 hours. The specific surface area was determined by the Brunauer–Emmett–Teller (BET) method. The

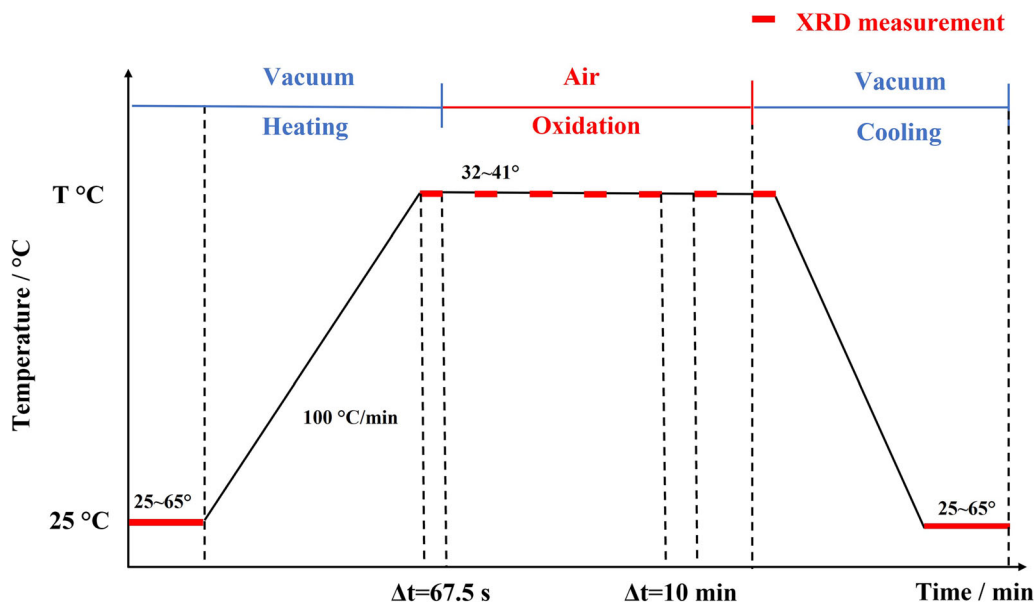


Fig. 1—Schematic diagram of HT-XRD measurements in the defined temperature.

cumulative pore volume, average pore diameter, and pore size distribution were analyzed using the Barrett–Joyner–Halenda (BJH) method.

III. RESULTS AND DISCUSSION

A. Oxidation Behavior by TGA Analysis

Figure 2 shows the oxidation TG-DTG curves of different samples. From Figure 2(a), it is obvious that sample B is the easiest to oxidize among the three samples. Based on the oxidation rate, as shown in Figures 2(b) through (d), the oxidation reaction can be divided into at least three oxidation stages. Peak 1 in all the samples locates at around 330 °C. At the temperature around peak 1, the oxidation mainly occurs at the surface of particles and the oxidation rate is limited by chemical reaction.^[33] The diffusion of Fe^{2+} and Fe^{3+} ions is also limited due to the low oxidation temperature. Therefore, the height of peak 1 is relatively low. The oxidation product is supposed to be $\gamma\text{-Fe}_2\text{O}_3$.^[30,45,46] At the temperature around peak 2 (550 °C), the $\gamma\text{-Fe}_2\text{O}_3$ becomes unstable and transforms

to $\alpha\text{-Fe}_2\text{O}_3$.^[37] From the kinetic point of view, the rate-limiting step for oxidation of magnetite in particle scale is solid-state diffusion. The diffusion rate constant is independent of oxygen partial pressure but increases with the temperature.^[37] The increasing temperature speeds up the diffusion of Fe^{2+} and Fe^{3+} ions and, hence, increases the oxidation rate. However, with the oxidation reaction proceeding, the formed $\alpha\text{-Fe}_2\text{O}_3$ shell blocks the diffusion of the iron and oxygen ions, which results in the decrease of the oxidation rate.^[47] At higher temperatures, the following peaks (peak 3 or 4) of different samples show diversities, which can be explained by the side reactions between impurities and iron oxides. The isomorphous substitution occurs widely in the structure of magnetite-based ores, resulting in an impurity element existing in the lattice of magnetite.^[48]

To comprehensively evaluate the oxidation behavior of different samples, the oxidation capacity index (OCI) is introduced. By analogy with the definition of the comprehensive combustion property index (S)^[49] of coal, the OCI of magnetite-based iron ore is calculated as Eqs. [2] through [7]:

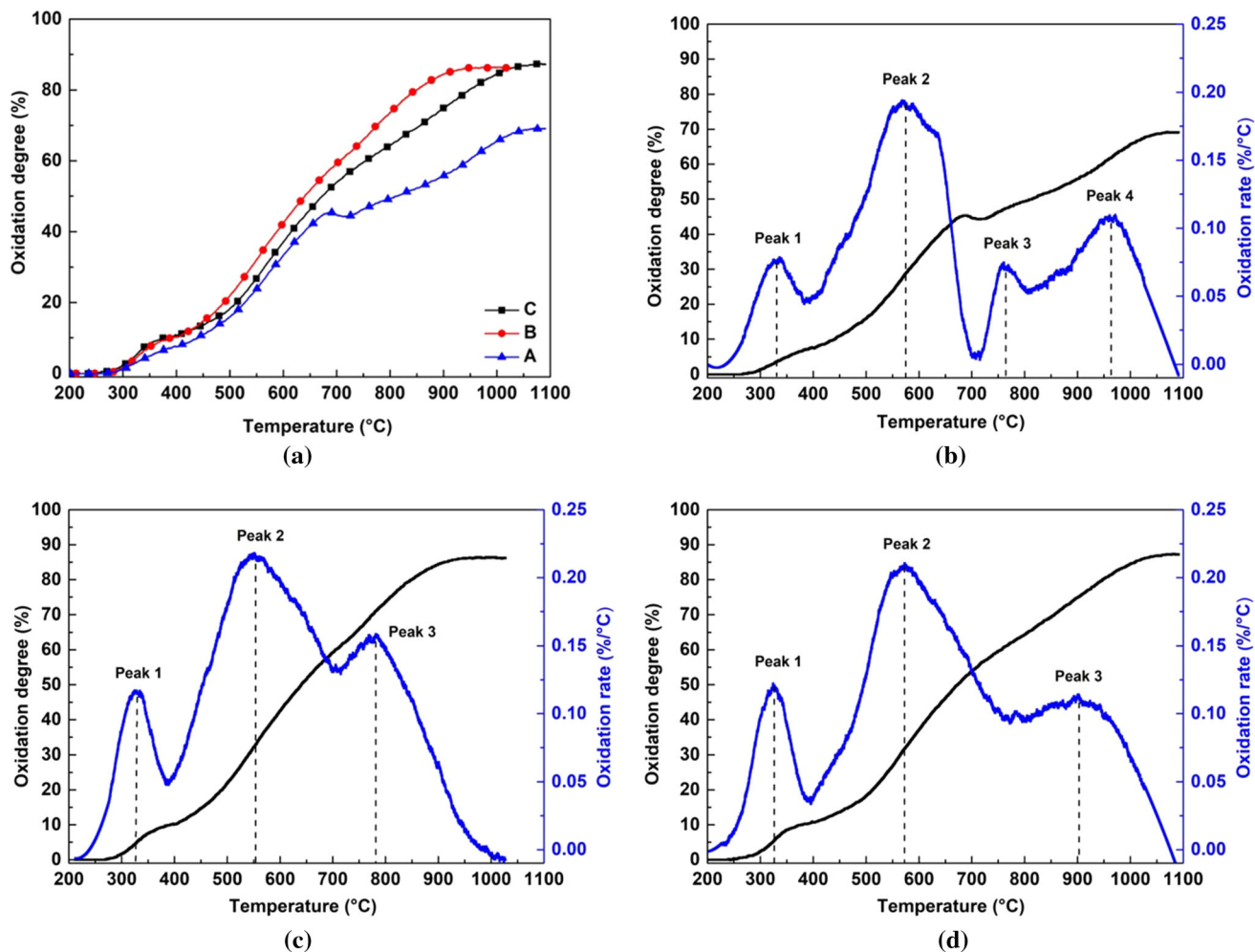


Fig. 2—Oxidation TG-DTG curves of the samples: (a) TG curve of samples, (b) TG-DTG curve of sample A, (c) TG-DTG curve of sample B, and (d) TG-DTG curve of sample C.

$$\frac{dw}{dt} = A \cdot \exp\left(-\frac{E}{RT}\right), \quad [2]$$

$$\frac{d}{dT}\left(\frac{dw}{dt}\right) = A \cdot \exp\left(-\frac{E}{RT}\right) \cdot \frac{E}{RT^2}. \quad [3]$$

Insert Eq. [3] into Eq. [2]:

$$\frac{R}{E} \frac{d}{dT}\left(\frac{dw}{dt}\right) = \left(\frac{dw}{dt}\right) \frac{1}{T^2}. \quad [4]$$

When oxidation starts, $T = T_i$:

$$\frac{R}{E} \frac{d}{dT}\left(\frac{dw}{dt}\right)_{T=T_i} = \left(\frac{dw}{dt}\right)_{T=T_i} \frac{1}{T_i^2} \quad [5]$$

Equation [6] is obtained from Eq. [5]:

$$\begin{aligned} \frac{R}{E} \frac{d}{dT}\left(\frac{dw}{dt}\right)_{T=T_i} &= \frac{(\frac{dw}{dt})_{max} (\frac{dw}{dt})_{mean}}{(\frac{dw}{dt})_{T=T_i} T_e} \\ &= \frac{(\frac{dw}{dt})_{max} (\frac{dw}{dt})_{mean}}{T_i^2 T_e}, \end{aligned} \quad [6]$$

where $\frac{d}{dT}\left(\frac{dw}{dt}\right)_{T=T_i}$ indicates the oxidation rate of the magnetite at the initial oxidation temperature; $\frac{(\frac{dw}{dt})_{max}}{(\frac{dw}{dt})_{T=T_i}}$ is the ratio of the maximum reaction rate and the initial reaction rate; and $\frac{(\frac{dw}{dt})_{mean}}{T_e}$ is the ratio of the mean reaction rate and the reaction finishing temperature T_e , which indicates the overall oxidation rate.

The right side of formula [6] is defined as the OCI:

$$OCI = \frac{(\frac{dw}{dt})_{max} (\frac{dw}{dt})_{mean}}{T_i^2 T_e} \quad [7]$$

The characteristic parameters of the oxidation are listed in Table III. T_i is the temperature when the oxidation starts. The temperature when sample B starts to be oxidized is much lower than that of samples A and C. T_{p-1} , T_{p-2} , T_{p-3} , and T_{p-4} are the temperatures of the peaks in the DTG curves. The highest oxidation rate of these three samples is in the temperature range of 548 °C

to 573 °C. The temperature of the second highest oxidation rate is in the range of 764 °C to 902 °C. The OCI represents the OCI of magnetite-based iron ore. A higher OCI value for a magnetite-based ore indicates that it is easier to oxidize. Sample B shows the highest OCI, followed by samples C and A.

B. Structural Evolution

1. Morphology analysis

The morphologies of the raw samples A, B, and C are shown in Figures 3 through 5, respectively. The surface morphologies of all the samples are similar. They are smooth and compact, with sharp edges. From SEM images, few gangues can be observed in sample A. However, the gangues are widely spread in samples B and C. As shown in Figures 4(c) and (d), the SiO₂ is the main impurity phase in sample B and is intertwined with the magnetite phase. As shown in Figures 5(c) and (d), the SiO₂ is also the main gangue in sample C but dotted with Ca, Al, and Na impurities. The SEM-ESD analysis is coincident with the chemical analysis that is shown in Table I.

Figure 6 shows the oxidation results of the isothermal oxidation tests, which give a similar trend as observed during the TGA tests. Within the same duration time, sample B shows the highest oxidation degree followed by samples C and A. The surface morphologies under different duration times are shown in Figures 7 through 9. As shown in Figures 7(b), 8(b), and 9(b), after only 2 minutes, the dense surface structure becomes rough and presents a nanosized gridlike structure. This phenomenon also occurred during the oxidation of vanadium-titanium magnetite ores.^[43,50,51] The gridlike structures are supposed to be hematite phase and caused by the out-diffusion of Fe²⁺. After 5 minutes, as shown in Figures 7(c), 8(c), and 9(c), the gridlike structures in sample B are much bigger than those in the other two samples. The gridlike structures in sample A are slightly bigger than those in sample C. According to Table I, sample B contains fewer impurity elements, while sample C has the most impurities. The impurity elements might replace the iron ions in the lattice and influence the diffusion of the cations. It can be suggested

Table III. Characteristic Parameters of the Oxidation

Parameters	Sample A	Sample B	Sample C
T_i (°C)	265	214	239
T_{p-1} (°C)	337	325	326
T_{p-2} (°C)	570	548	573
T_{p-3} (°C)	764	778	902
T_{p-4} (°C)	962	—	—
T_e (°C)	1083	1000	1091
$(\frac{dw}{dt})_{max-1}$ (pct/min)	0.5663	0.8719	0.9050
$(\frac{dw}{dt})_{max-2}$ (pct/min)	1.4375	1.6143	1.5784
$(\frac{dw}{dt})_{max-3}$ (pct/min)	0.5318	1.1468	0.8558
$(\frac{dw}{dt})_{max-4}$ (pct/min)	0.7971	—	—
$(\frac{dw}{dt})_{mean}$ (pct/min)	0.4778	0.6470	0.5998
$OCI \times 10^{-8}$ (pct ² min ⁻² °C ⁻³)	0.9031	2.2807	1.5192

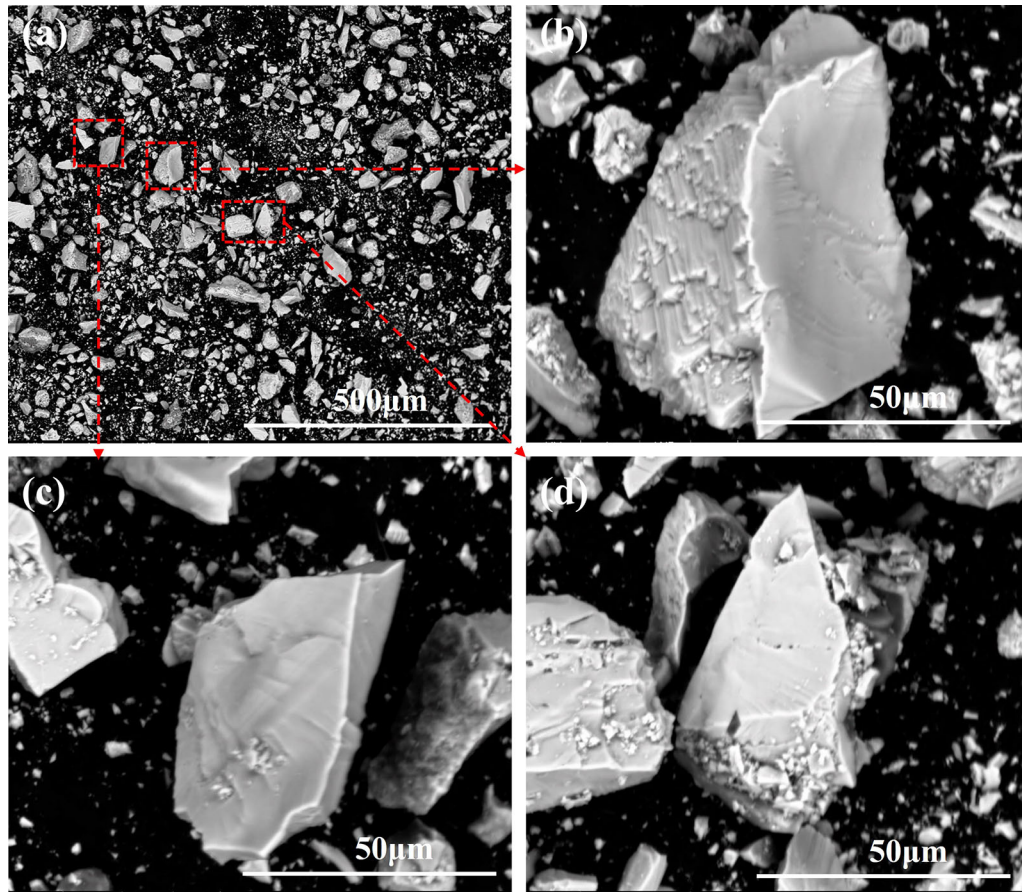


Fig. 3—Surface morphology of raw sample A under SEM: (a) through (d) different magnification times.

that these impurity elements influence the diffusion of the iron ions, resulting in the different growth behavior of the gridlike structures. With the oxidation time, the gridlike structures grow bigger and connect with each other.

2. Internal structure evolution

To investigate the evolution of the internal structure, the samples under different duration times are observed, as shown in Figure 10. All the raw magnetite samples show compact structures. These three samples follow a similar oxidation path: surface oxidation to internal oxidation. As shown in Figures 10(b), (f), and (j), the oxidation first occurs at the surface of the magnetite particle. Then, with increasing oxidation time, as shown in Figures 10(c), (g), and (k), obvious hematite shells are formed. In the final oxidation stage, as shown in Figures 10(d), (h), and (l), the hematite shell does not grow uniformly inward toward the magnetite core. Instead, the needlelike hematite structures originate from the surface hematite shell and grow inside the particle. It should be noted that no pores or cracks can be observed in the boundaries between the hematite and

magnetite phases. The oxidized samples still show compact structures. The oxidation mechanism is introduced in Section II-F.

C. Pore Structure Parameters Based on N_2 Adsorption

1. Specific surface area and pore volume

In this study, BET and BJH methods are used to investigate the pore structures during the oxidation of magnetite-based iron ores. The results of the pore structure parameters are listed in Table IV. The specific areas of the raw samples A, B, and C are 1.63, 0.94, and 0.83 m^2/g , respectively. After 5 minutes of oxidation, the specific surface areas decrease significantly to 0.52, 0.38, and 0.29 m^2/g , which can be explained by the sintering effect at the high temperature. With the oxidation time, the specific areas keep decreasing. The total pore volumes of all the samples show the same trend as their specific areas. However, the average pore sizes of the samples keep increasing with the oxidation. This is due to the closure of the small pores, which is caused by the sintering effect. It should be noted that sample B shows the biggest specific area and pore volume after 60

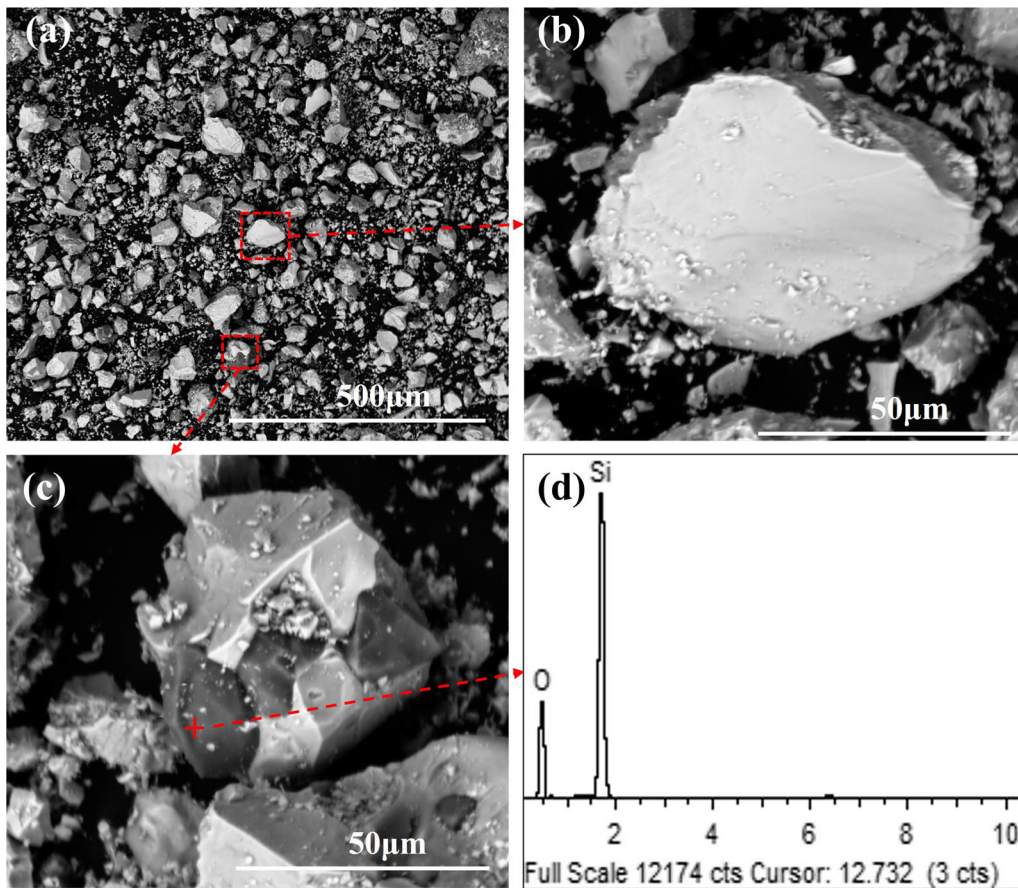


Fig. 4—Surface morphology of raw sample B under SEM: (a) through (c) different magnification times and (d) EDS analysis of the gangue.

minutes of oxidation, which may contribute to its high oxidation rate in the late oxidation process.

2. Pore size distribution

The pore size distributions of the samples within different duration times are shown in Figure 11. For the raw samples, the dominant pore size is between around 2 and 5 nm. For the oxidized samples, the pore size that is smaller than 3 nm decreases significantly. This phenomenon confirms the sintering effect.

D. HT-XRD Analysis

The HT-XRD patterns of the samples present similar characteristics. Therefore, as an example, only the patterns of sample B are shown in Figure 12. The appearance of Pt peaks in Figure 12 is because of the platinum heating strip. The HT-XRD results reveal that the temperature is one of the major factors influencing the oxidation of magnetite. At 400 °C, as shown in Figure 12(a), a small hematite peak appears after 10 minutes. However, the relative intensities of the hematite peaks remain stable afterward, which

illustrates that the amount of the hematite phase does not increase. At 600 °C, as shown in Figure 12(b), the relative intensities of the hematite peaks grow with the duration time. At 800 °C and 1000 °C, the oxidation of the sample proceeds quickly. After 10 minutes, the peaks of the magnetite phase are hardly observed.

Bhargava *et al.*^[44] normalized the relative intensity of the strongest peaks of the magnetite, hematite, and pyrite phases, respectively, to investigate the phase transformation of pyrite at high temperature. It should be noted that the relative peak intensity of each phase is not proportional to its content. In this study, a similar method, named the matrix-flushing method,^[52,53] is used to conduct the quantitative analysis. The intensity of phase j can be expressed as

$$I_j = \frac{C_j \cdot x_j}{\rho_j \cdot \mu_m}, \quad [8]$$

where C_j is the structure factor, x_j is the proportion of phase j in the mixture phases, ρ_j is the density of phase j , and μ_m is the mass absorption coefficient of the mixture phases.

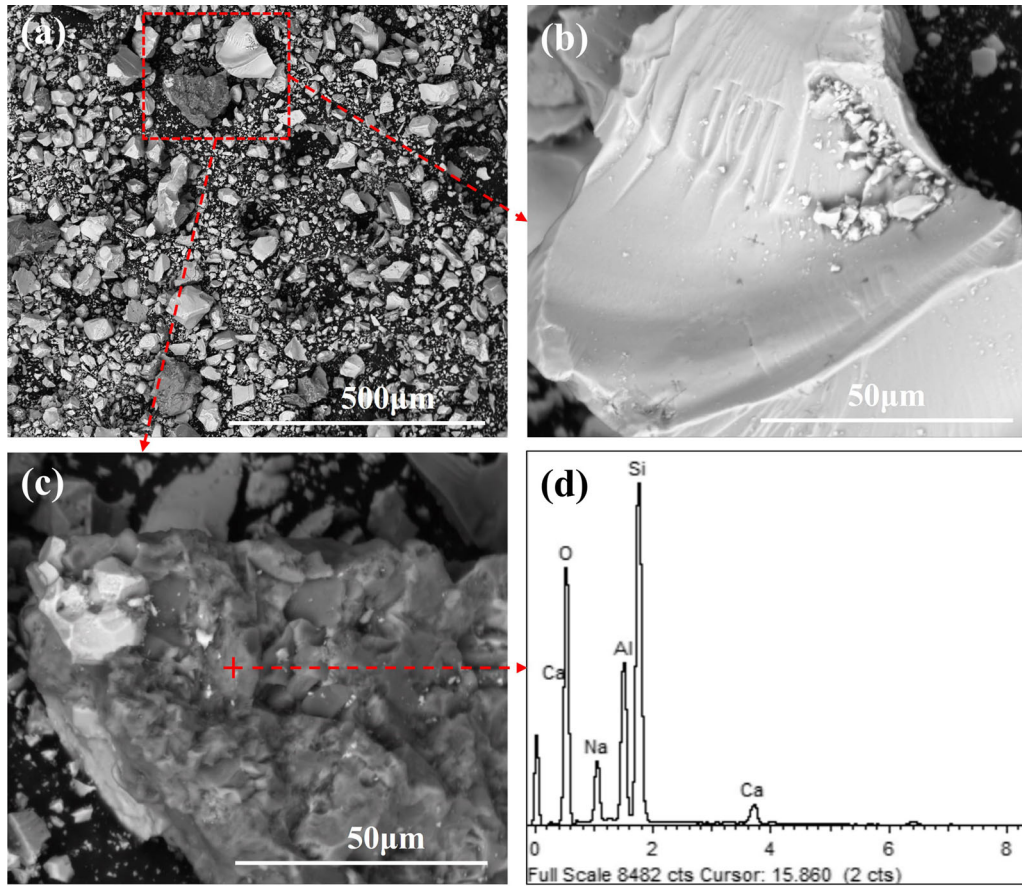


Fig. 5—Surface morphology of raw sample C under SEM: (a) through (c) different magnification times and (d) EDS analysis of the gangue.

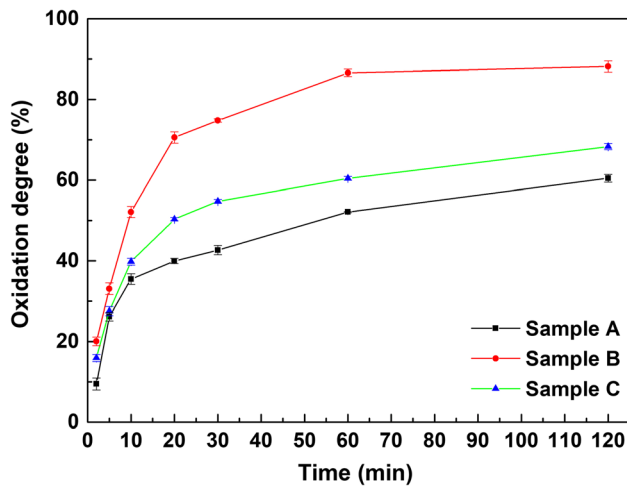


Fig. 6—Oxidation degree within certain duration times.

Assuming that phase j is a certain reference phase, phase i can be calculated.

$$I_j/I_i = \frac{C_j \cdot x_j / \rho_j \cdot \mu_m}{C_i \cdot X_i / \rho_i \cdot \mu_m} \quad [9]$$

Since C_j , C_i , ρ_j , ρ_i , and μ_m are constant, $\frac{C_j}{\rho_j \cdot \mu_m}$ and $\frac{C_i}{\rho_i \cdot \mu_m}$ can be defined as k_j and k_i , respectively. Therefore, the proportion of phases i and j can be calculated based on Eqs. [10] and [11]:

$$x_i/x_j = \frac{I_i}{k_i} / \frac{I_j}{k_j}, \quad [10]$$

$$x_i + x_j = 1, \quad [11]$$

where I_i is the intensity of phase I and k_j is the relative intensity ration (RIR). The RIR of each phase can be found in the PDF card database. The RIRs of the magnetite and hematite phases are 4.9 and 3.2, respectively.

The magnetite and hematite peaks located at around 35 deg overlap each other. To distinguish and split each peak, the XRD pattern is refined by Jade 6.0. Figure 13 shows an example of the XRD patterns after refinement. In this way, the relative content of the magnetite and hematite can be calculated. The results are shown in Figure 14. The result is consistent with the TGA test that demonstrates that sample B is the easiest one to oxidize. The oxidation of magnetite proceeds relatively

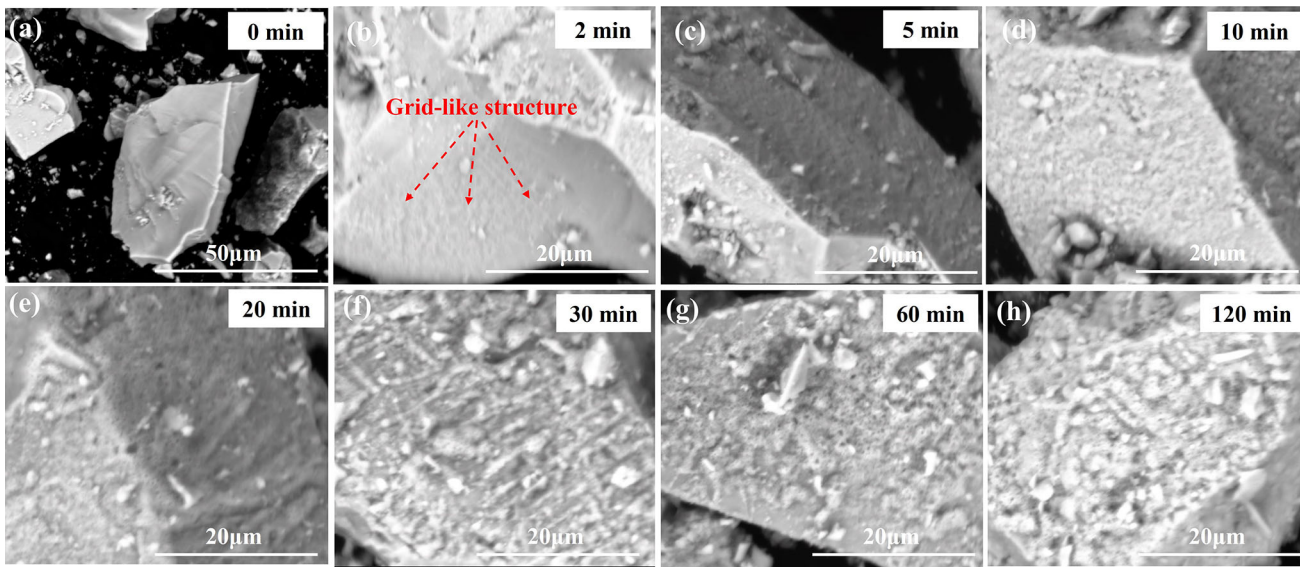


Fig. 7—SEM images of the oxidized products of sample A obtained under different duration times: (a) 0 min, (b) 2 min, (c) 5 min, (d) 10 min, (e) 20 min, (f) 30 min, (g) 60 min, and (h) 120 min.

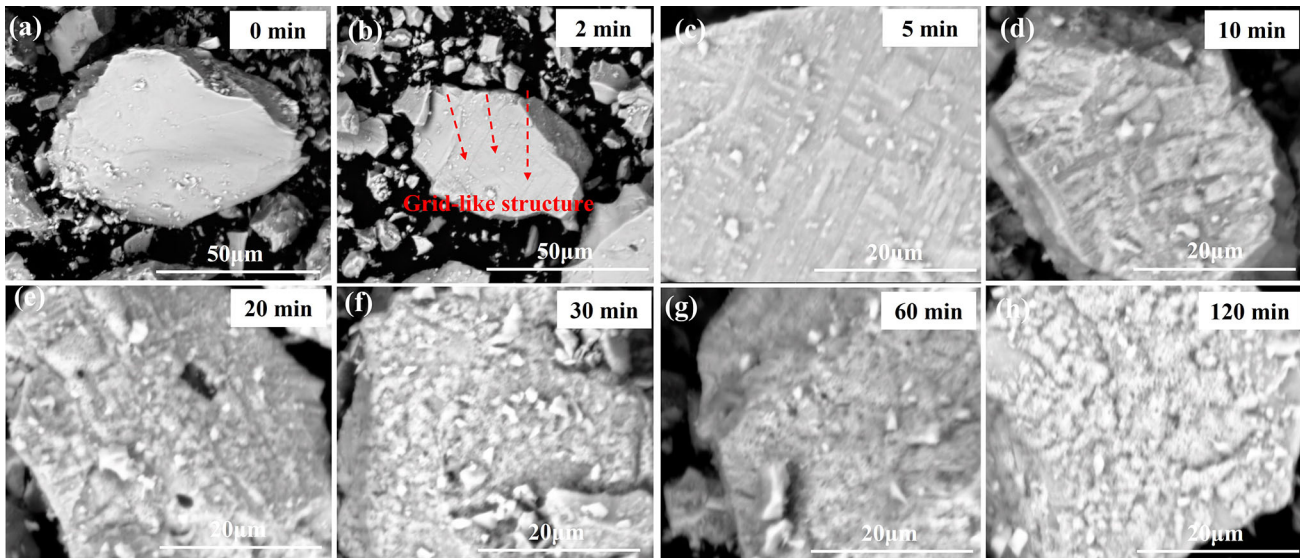


Fig. 8—SEM images of the oxidized products of sample B obtained under different duration times: (a) 0 min, (b) 2 min, (c) 5 min, (d) 10 min, (e) 20 min, (f) 30 min, (g) 60 min, and (h) 120 min.

slowly at 400 °C and 600 °C. When the temperature is increased to 800 °C and above, the oxidation rate increases significantly.

E. First-Principles Calculation

From the observation of the hematite structure, discussed in Section II-B, it seems that the hematite phase shows a certain growth habit. Yang and co-workers^[54,55] studied the effects of SiO₂ and Al₂O₃ on the

growth habit of calcium ferrite based on the surface energy (SE) by the first-principles calculation method. The growth rates of the crystal faces are proportional to their surface energies. Based on our previous studies,^[54,55] the preferred growth orientation of the hematite phase is calculated using the same method and calculation parameters. Figure 15 shows the HT-XRD patterns of sample B under 600 °C and 800 °C without normalization. The hematite crystal face (104) shows quite high intensity after 10 minutes and the

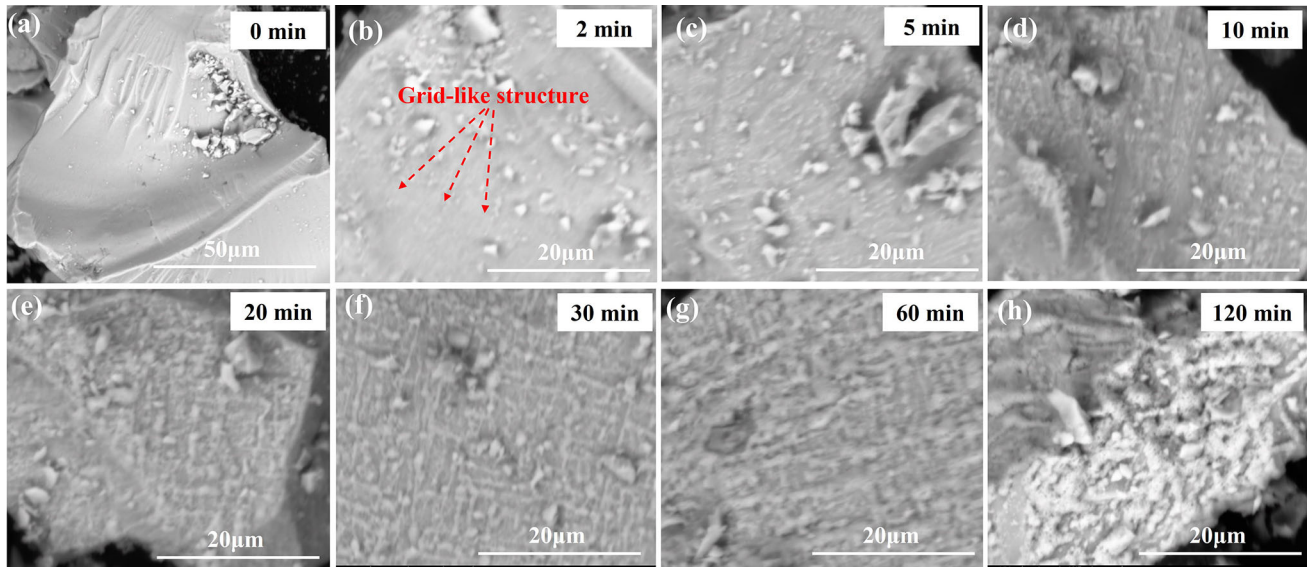


Fig. 9—SEM images of the oxidized products of sample C obtained under different duration times: (a) 0 min, (b) 2 min, (c) 5 min, (d) 10 min, (e) 20 min, (f) 30 min, (g) 60 min, and (h) 120 min.

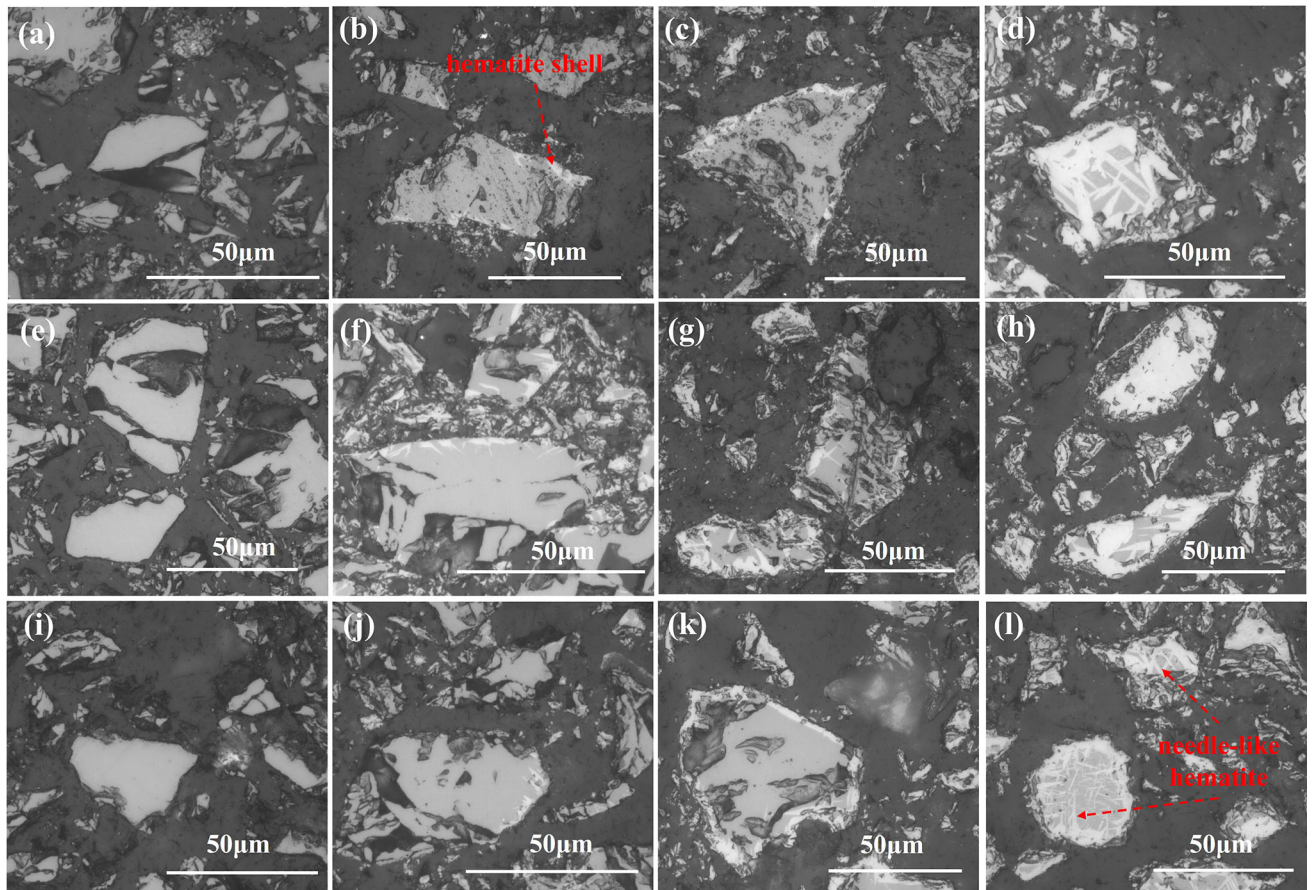


Fig. 10—Polished section images of the oxidized samples obtained under different duration times: (a) through (d) sample A under 0, 2, 5, and 60 min; (e) through (h) sample B under 0, 5, 30, and 120 min; and (i) through (l) sample C under 0, 2, 30, and 120 min.

Table IV. Pore Structure Parameters of Samples Within Different Duration Times

Duration Time (Min)	Sample A			Sample B			Sample C		
	Average Pore Size (nm)	Total Pore Volume ($\times 10^{-4}$ cm ³ /g)	Specific Surface Area (m ² /g)	Average Pore Size (nm)	Total Pore Volume ($\times 10^{-4}$ cm ³ /g)	Specific Surface Area (m ² /g)	Average Pore size (nm)	Total Pore Volume ($\times 10^{-4}$ cm ³ /g)	Specific Surface Area (m ² /g)
0	4.93	16.03	1.63	5.30	9.23	0.94	4.60	7.12	0.83
5	5.94	6.53	0.52	5.60	4.34	0.38	6.80	3.28	0.29
10	5.79	7.50	0.54	5.60	3.16	0.27	6.10	2.62	0.23
20	5.87	7.80	0.55	5.87	3.12	0.27	9.88	1.78	0.18
60	6.13	2.46	0.24	5.70	3.16	0.30	10.61	1.34	0.16

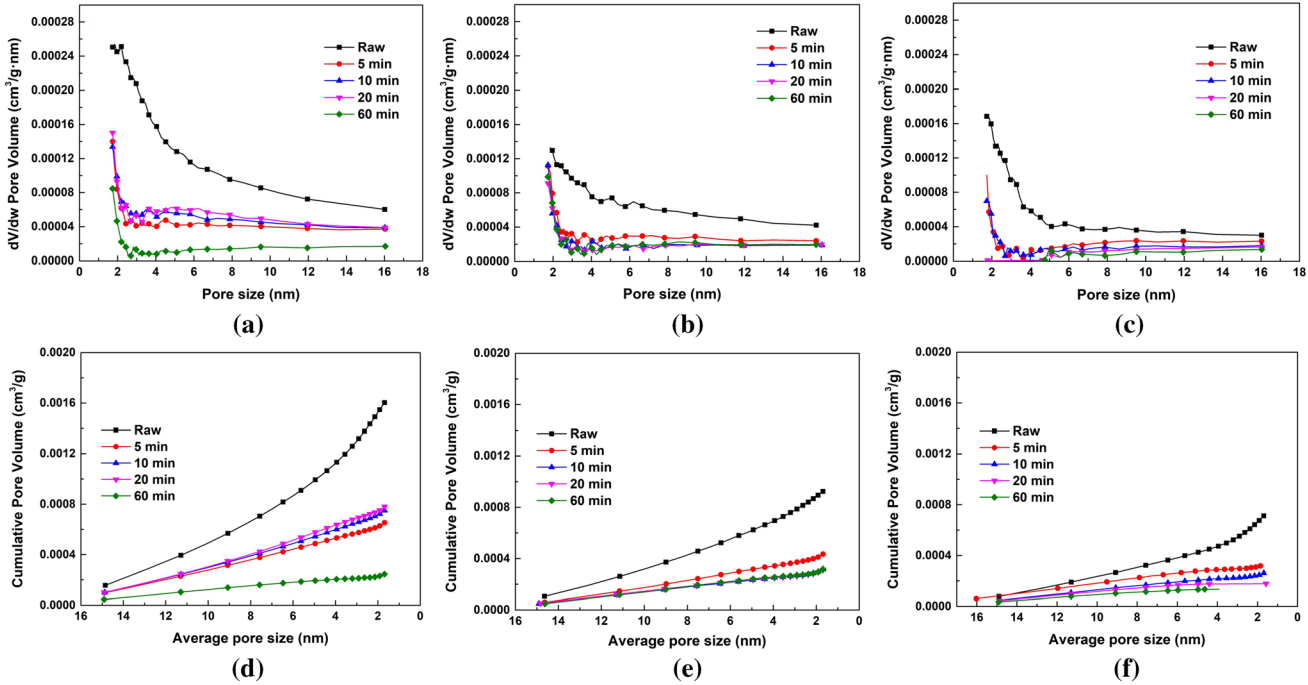


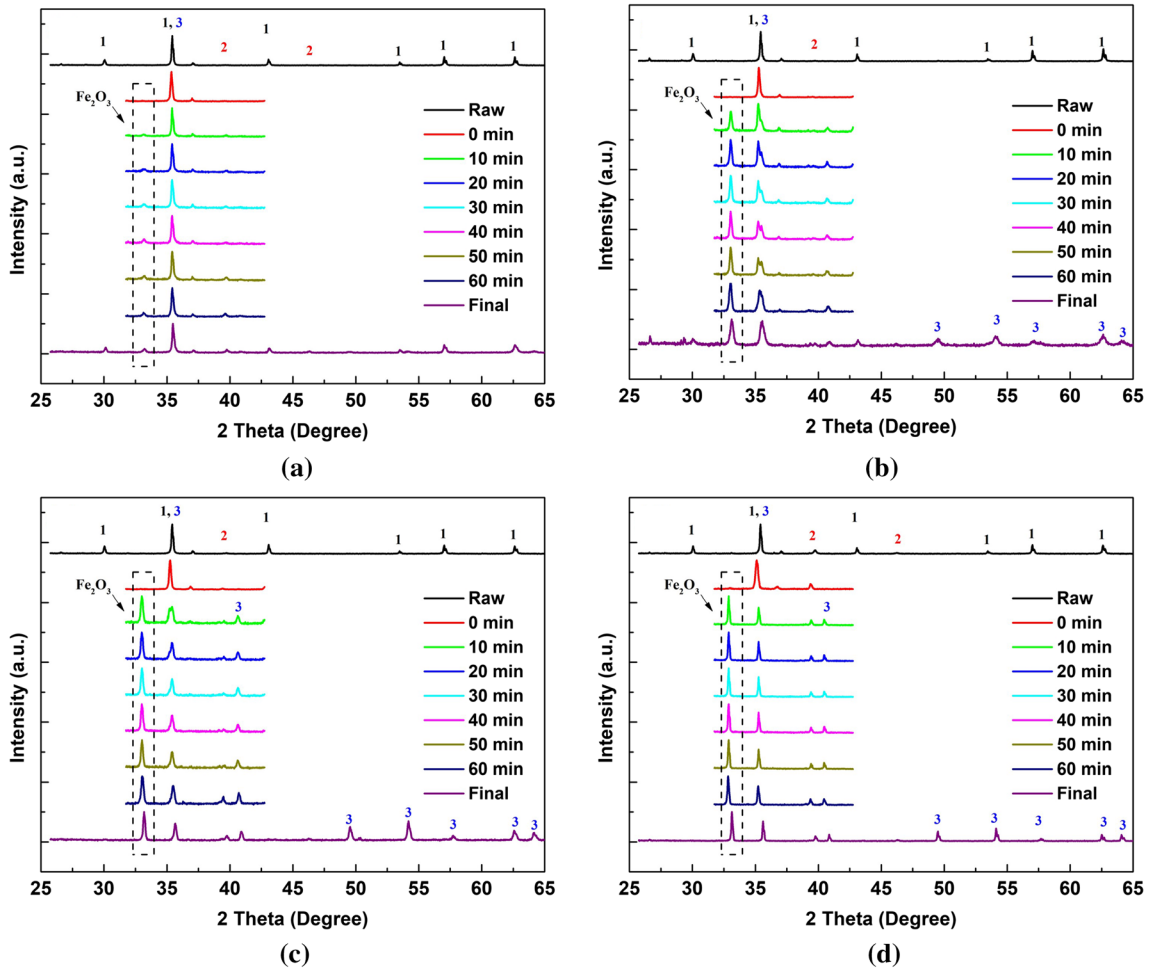
Fig. 11—Pore size distribution of the samples: (a) and (d) sample A, (b) and (e) sample B, and (c) and (f) sample C.

intensity is much larger than that of crystal faces (110) and (113). With the oxidation time, the intensities of (104) and (110) crystal face gradually increase. That is, the hematite phase has a preferred orientation along the (104) or (110) crystal face. The oxidation temperature difference showed no influence on the preferred orientation. The SE is calculated as shown in Eq. [12]:

$$SE = (E_{surface} - n \times E_{bulk}) / (2A), \quad [12]$$

where $E_{surface}$ and E_{bulk} are the total energy of the crystal surface model and the energy of the unit cell, respectively. A and n are the surface area of the crystal plane model and the number of the cells contained in the crystal plane model.

The model used for the calculation is shown in Figure 16. The calculated SE of each crystal face is shown in Figure 17. The SEs of the (104), (110), and (113) are 18.88, 27.37, and 15.59 eV/nm², respectively. The surface energies of the (104) and (110) crystal



1: Fe_3O_4 (PDF card No. 89-0688); 2: Pt (PDF card No. 04-0802); 3: Fe_2O_3 (PDF card No. 89-0597)

Fig. 12—*In-situ* HT-XRD patterns of sample B under different temperatures and duration times: (a) 400 °C, (b) 600 °C, (c) 800 °C, and (d) 1000 °C.

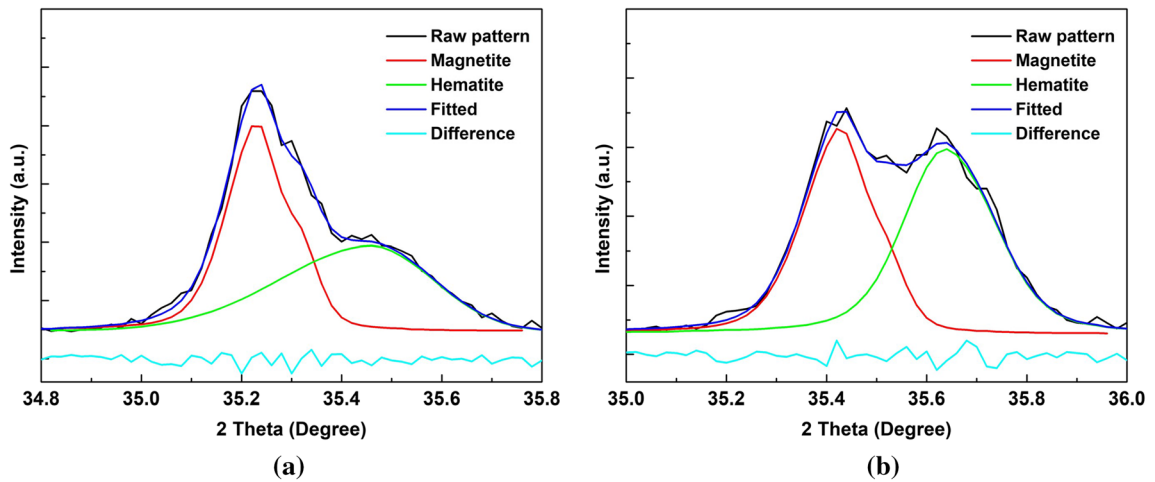


Fig. 13—Rietveld refinement profile of sample B for oxidation at 600 °C: (a) 10 min and (b) final.

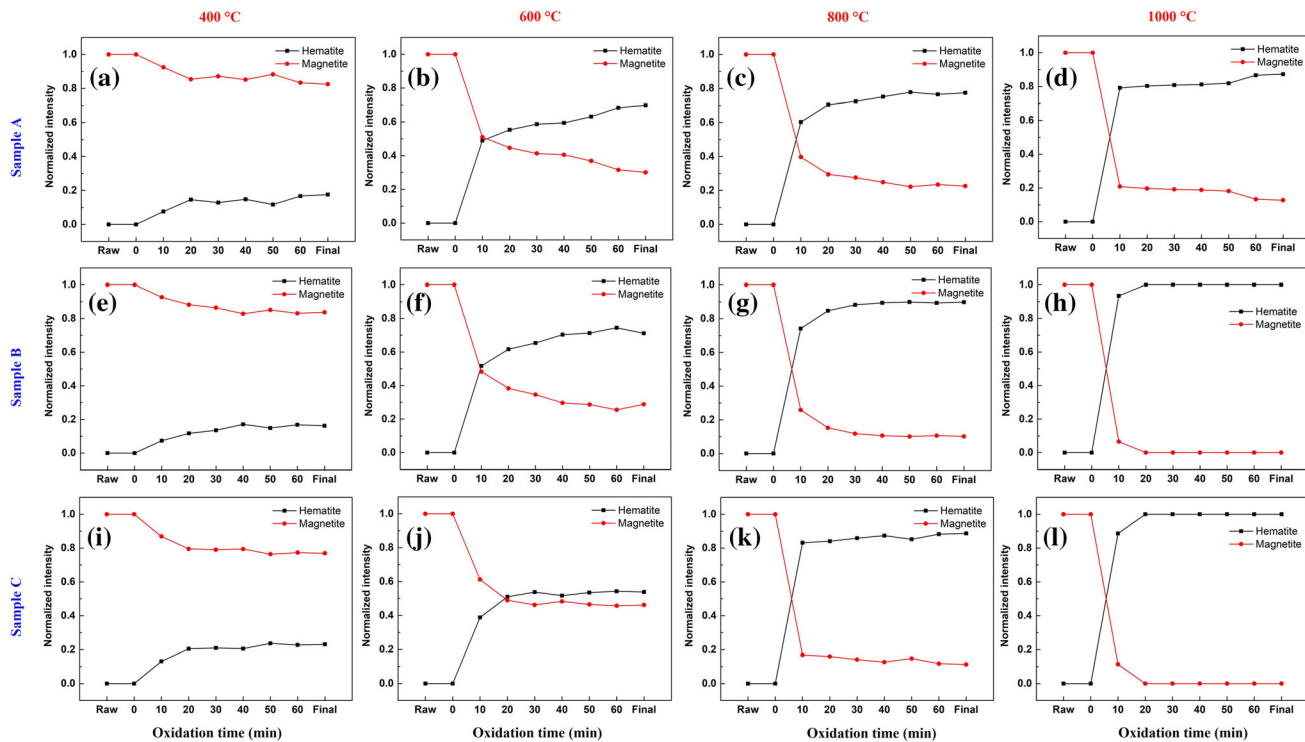


Fig. 14—Normalized intensities of the samples: (a) through (d) sample A under 400 °C, 600 °C, 800 °C, and 1000 °C; (e) through (h) sample B under 400 °C, 600 °C, 800 °C, and 1000 °C; (i) through (l) sample C under 400 °C, 600 °C, 800 °C, and 1000 °C.

surfaces are larger than that of the (113) crystal surface. Hence, the hematite crystals may preferentially orient themselves along the (104) or (110) crystal surface, which shows agreement with the HT-XRD results.

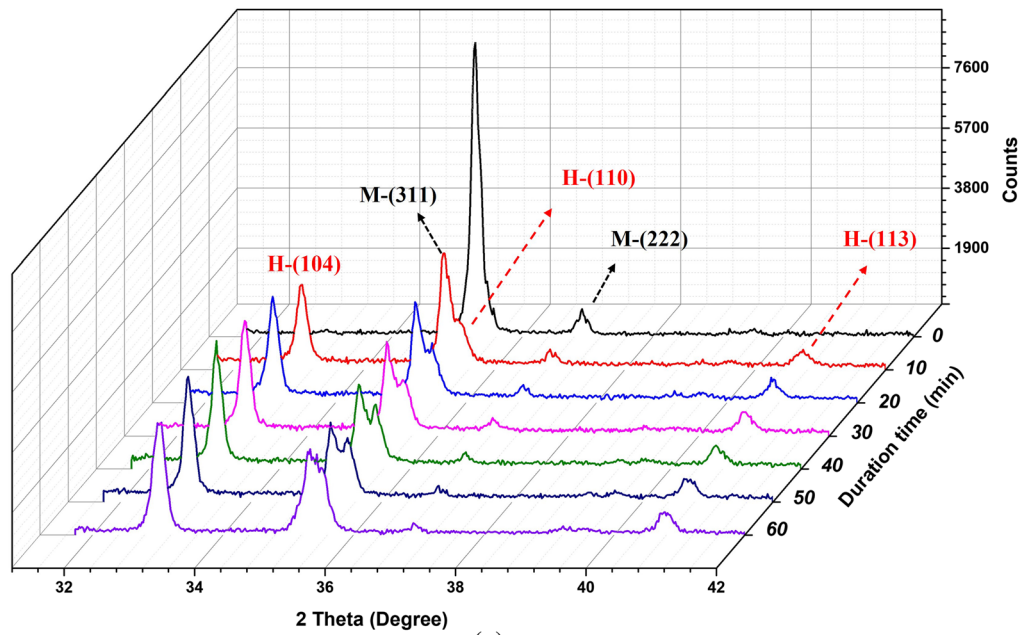
F. Oxidation Mechanism

The magnetite crystal unit has 32 oxygen anions and 24 iron cations (16Fe^{3+} and 8Fe^{2+}). The oxygen anions have a cubic close-packed structure in the magnetite unit. There are 96 interstices between the oxygen anions, of which 64 are tetrahedral interstices and 32 are octahedral interstices. Only eight tetrahedral interstices are occupied by Fe^{3+} cations. Sixteen of 32 octahedral interstices are occupied by 8Fe^{3+} cations and 8Fe^{2+} cations.^[56] As a result of such free interstices, the iron cations move more easily in the crystal lattice than oxygen anions.^[57] The size of an O^{2-} anion (1.26 Å) is much larger than that of an Fe^{2+} cation (0.75 Å) and Fe^{3+} cation (0.69 Å). Thus, the smaller size of the iron cation guarantees its predominant diffusion in the magnetite crystal unit.

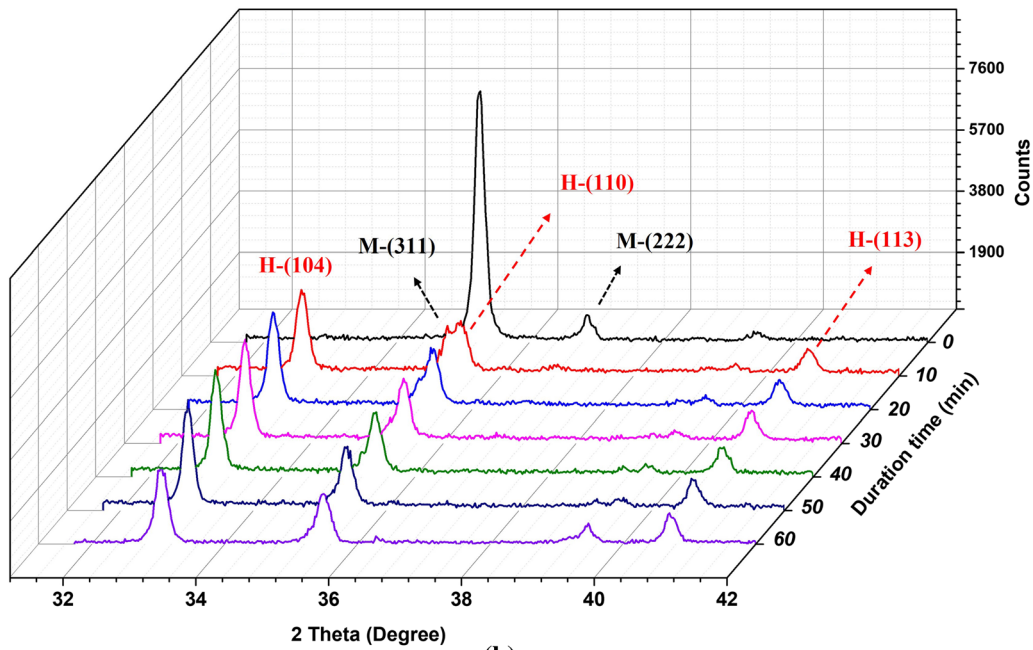
From the aspect of the crystal lattice, during the oxidation of magnetite, when an oxygen atom penetrates the magnetite lattice, two electrons are trapped. The local charges in the crystal must be neutral;

therefore, two positively charged holes, 2h^+ , are generated in the place of the previous electrons.^[58] Figure 18 shows the schematic of the oxidation mechanism. When the Fe^{2+} cation captures the charged hole h^+ , the valence increases and the iron becomes trivalent. However, in the later oxidation period, the charged hole h^+ has a greater opportunity to meet the Fe^{3+} cation. In this case, they are tantamount to an impurity cation with a higher valence ($>3^+$), which forces the lattice to become more compact.^[58] Hence, the mobility of the iron cations decreases significantly, resulting in a very slow oxidation rate of magnetite in the later stage.

From the aspect of a single magnetite particle, the oxidation first occurs at the surface and then extends inside. Figure 19 shows the oxidation process of a single magnetite particle. When the oxygen atoms capture the electrons from the magnetite phase, the oxidation occurs. The first hematite film appears in the interface. The Fe cations prefer to diffuse to the surface of the particle due to the low iron cation contents. The concentration gradient becomes the chemical drive for the outgrowth of the hematite. On the other hand, as discussed in Section II-E, the hematite phase has a preferred orientation along the (104) or (110) crystal face, which results in the formation of the gridlike structure at the surface. With the oxidation, the



(a)



(b)

Fig. 15—HT-XRD patterns of sample B without normalization: (a) under 600 °C and (b) under 800 °C. H and M represent hematite and magnetite, respectively.

hematite becomes the dominant phase at the surface. Then, the Fe^{3+} cations start to diffuse toward the particle center and form the needlelike hematite structures. The needlelike hematite structures grow and merge until the end of the oxidation.

IV. CONCLUSIONS

The purpose of this research is to investigate the oxidation of magnetite-based iron ore fines, which are helpful in optimizing the production of DRI by means of fluidized bed technology. Three magnetite-based iron

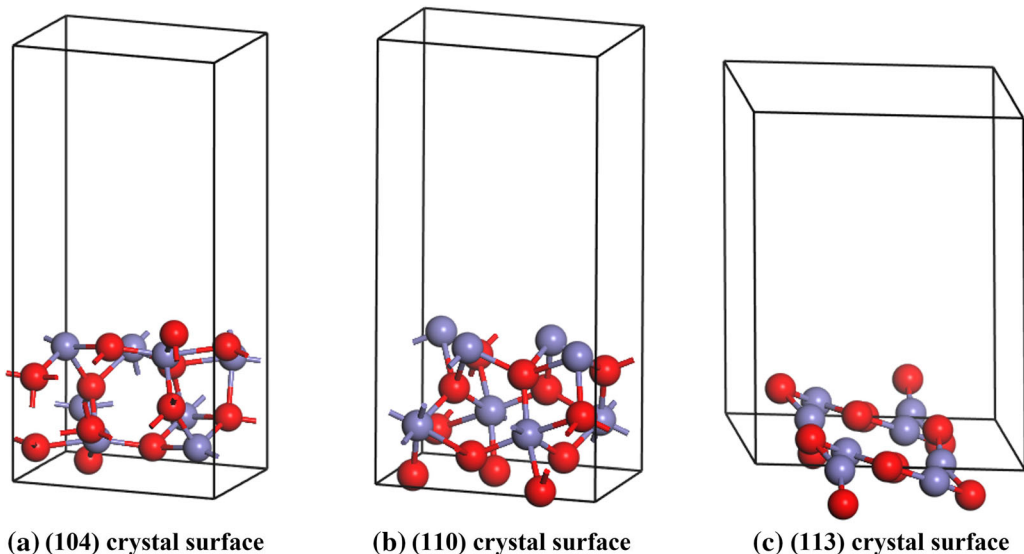


Fig. 16—Model used for the calculation (the red ball represents O ion; the purple ball represents Fe ion): (a) (104) crystal surface, (b) (110) crystal surface, and (c) (113) crystal surface.

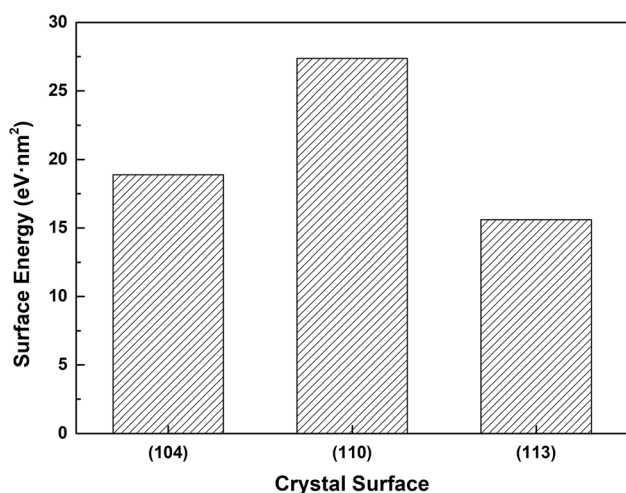


Fig. 17—Surface energies of the (104), (110), and (113) crystal surfaces.

ore brands are analyzed in terms of their oxidation characteristics, surface morphology, and structural evolution. The following conclusions are obtained.

1. According to nonisothermal oxidation DTA analysis, the oxidation reaction can be divided into at least three stages. The first two oxidation rate peaks are observed at around 330 °C and 550 °C, respectively, indicating the formation of γ -Fe₂O₃ and α -Fe₂O₃.

The highest oxidation rate of these three samples is in the temperature range between 548 °C and 573 °C. Sample B shows the highest OCI, followed by samples C and A. The magnetite-based iron ore with a higher OCI value is easier to oxidize.

2. During oxidation, the surface of all of the samples becomes rough and presents nanosized gridlike structure due to the outgrowth of hematite. The gridlike structures of sample B are much bigger than those in the other two samples. Sample B contains fewer impurity elements, while sample C contains the most impurities. It seems that these impurity elements influenced the diffusion of the iron ions, resulting in the different growth behaviors of the gridlike structures. With oxidation time, the gridlike structures grow bigger and connect with each other. At the same time, the hematite phase also grows in the particle, forming the needlelike structures.
3. The specific surface areas of samples A, B, and C decrease significantly after only 5 minutes of oxidation—from 1.63, 0.94, and 0.83 m²/g to 0.52, 0.38, and 0.29 m²/g, respectively. With the oxidation time, the specific areas keep decreasing. The total pore volumes of all the samples show the same trend as their specific areas. Compared with the raw samples, the pore size smaller than 3 nm in the oxidized sample is significantly reduced.
4. The hematite phase shows a certain growth habit. Based on HT-XRD patterns, the hematite crystal

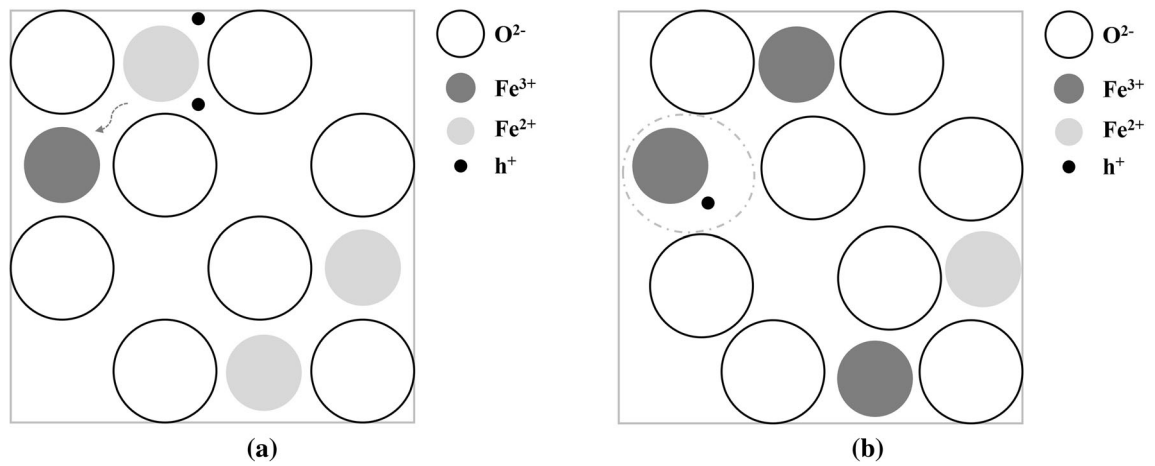


Fig. 18—Schematic of the oxidation mechanism of magnetite: (a) the Fe^{2+} cation turns into the Fe^{3+} cation and (b) later oxidation period.

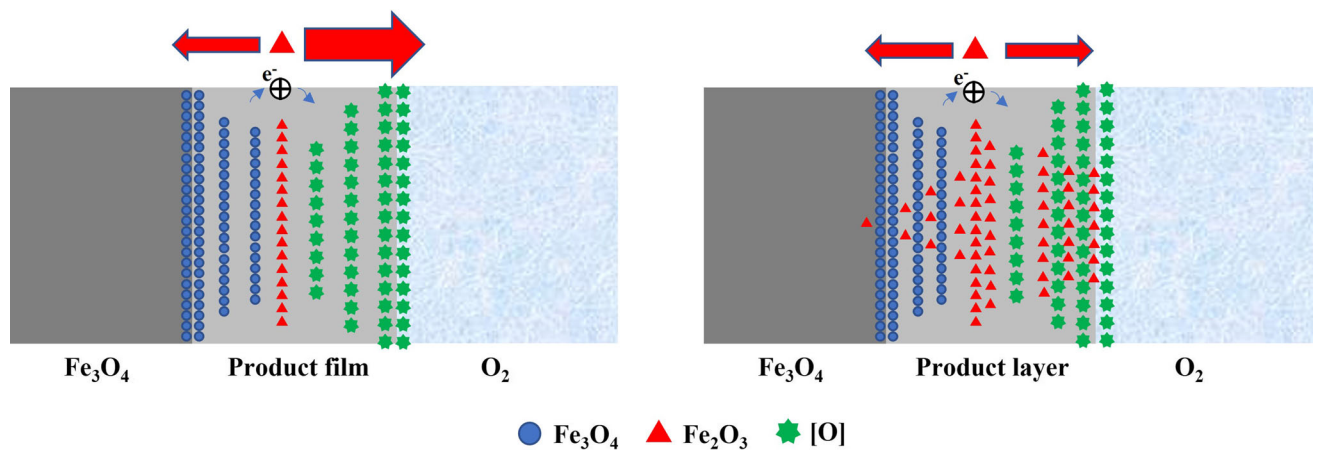


Fig. 19—Oxidation process of a single magnetite particle.

face (104) shows quite high intensity after 10 minutes of oxidation and the intensity is much larger than that of crystal faces (110) and (113). With the oxidation time, the intensities of (104) and (110) crystal faces gradually increase. The first-principles calculation confirms the preferential orientation. Theoretically, the surface energies of the (104) and (110) crystal surfaces are larger than that of the (113) crystal surface. Hence, the hematite crystals may preferentially orient themselves along the (104) or (110) crystal surface.

ACKNOWLEDGMENTS

The authors gratefully acknowledge the funding support of K1-MET GmbH, metallurgical competence center. The research program of the K1-MET competence center is supported by COMET (Competence Center for Excellent Technologies), the Austrian program for competence centers. COMET is funded by the Federal Ministry for Climate Action, Environ-

ment, Energy, Mobility, Innovation and Technology; the Federal Ministry for Digital and Economic Affairs; the provinces of Upper Austria, Tyrol, and Styria; and the Styrian Business Promotion Agency (SFG). In addition, the research work is partially financed by Montanuniversitaet Leoben. One of the authors (ZH) greatly acknowledges the financial support from the China Scholarship Council program (Grant No. 201908420284).

CONFLICT OF INTEREST

On behalf of all of the authors, the corresponding author states that there is no conflict of interest.

FUNDING

Open access funding provided by Montanuniversität Leoben.

OPEN ACCESS

This article is licensed under a Creative Commons Attribution 4.0 International License, which permits use, sharing, adaptation, distribution and reproduction in any medium or format, as long as you give appropriate credit to the original author(s) and the source, provide a link to the Creative Commons licence, and indicate if changes were made. The images or other third party material in this article are included in the article's Creative Commons licence, unless indicated otherwise in a credit line to the material. If material is not included in the article's Creative Commons licence and your intended use is not permitted by statutory regulation or exceeds the permitted use, you will need to obtain permission directly from the copyright holder. To view a copy of this licence, visit <http://creativecommons.org/licenses/by/4.0/>.

REFERENCES

1. B. McNab, A. Jankovis, D. David, and P. Payne: *Proc. Iron Ore Conf.*, The Australasian Institute of Mining and Metallurgy (The AusIMM), Perth, Australia, 2009, pp. 1–12.
2. Department of the Premier and Cabinet: *South Australia's Magnetite Strategy: Making Our State's Magnetite the World's Choice for Steelmaking*, p. 7, <https://sarigbasis.pir.sa.gov.au/WebtopEw/ws/samref/sarigl/image/DDD/BROCH028.pdf>. Accessed September 16, 2021.
3. L. Blaney: *Magnetite (Fe₃O₄): Properties, Synthesis, and Applications*, 2007, pp. 36–39, https://scholar.google.com/scholar?hl=en&as_sdt=0%2C5&q=Magnetite+%28Fe3O4%29%3A+Properties%2C+synthesis%2C+and+applications%2C&btnG=. Accessed September 16, 2021.
4. D. Zhu, J. Pan, L. Lu, and R.J. Holmes: *Iron Ore*, Processing and Environmental Sustainability, Woodhead Publishing, Sawston, England, Mineralogy, 2015, pp. 435–73.
5. H. Han and L. Lu: *Miner. Process. Extr. Metall. Rev.*, 2018, vol. 39, pp. 217–30.
6. S. Purohit, G. Brooks, M.A. Rhamdhani, M.I. Pownceby, and N.A.S. Webster: *Ironmak. Steelmak.*, 2020, vol. 47, pp. 674–85.
7. S. Purohit, G. Brooks, M.A. Rhamdhani, M.I. Pownceby, and N.A.S. Webster: *Ironmak. Steelmak.*, 2020, vol. 47, pp. 852–64.
8. S. Purohit, M.A. Rhamdhani, and G. Brooks: *AISTech Conf.*, Philadelphia, PA, 2018, pp. 1–8.
9. D. Zhu, V. Mendes, T. Chun, J. Pan, Q. Li, J. Li, and G. Qiu: *ISIJ Int.*, 2011, vol. 51, pp. 214–19.
10. X. Jiang, L. Wang, and F.M. Shen: *Adv. Mater. Res.*, 2013, vol. 805–806, pp. 654–59.
11. K. Huitu, M. Helle, H. Helle, M. Kekkonen, and H. Saxén: *Steel Res. Int.*, 2015, vol. 86, pp. 456–65.
12. World Steel Association: *Climate Change Mitigation*, http://www.acer.org.ar/wp-content/uploads/2019/07/fact20sheet_climate20mitigation_2019_vfinal.pdf. Accessed September 16, 2021.
13. European Commission: *2050 Long-Term Strategy—Climate Action—European Commission*, https://ec.europa.eu/clima/policies/strategies/2050_en. Accessed September 16, 2021.
14. A. Toktarova, I. Karlsson, J. Rootzén, L. Göransson, M. Odenberger, and F. Johnsson: *Energies.*, 2020, vol. 13, p. 3840.
15. SALCOS: SALCOS Official webpage, <https://salcos.salzgitter-ag.com/en/>. Accessed September 16, 2021.
16. V. Vogl, M. Åhman, and L.J. Nilsson: *J. Cleaner Prod.*, 2018, vol. 203, pp. 736–45.
17. M. Axelson, I. Robson, T.G. Wyns, and G.A. Khandekar: *Breaking Through—Industrial Low-CO₂ Technologies on the Horizon (2018)*, The Institute for European Studies (IES), p. 52. <https://researchportal.vub.be/en/publications/breaking-through-industrial-low-co2-technologies-on-the-horizon>. Accessed September 16, 2021.
18. Daniel Spreitzer: Ph.D. Thesis, Montanuniversität Leoben, Leoben, Austria, unpublished research, 2020.
19. H. Zheng, D. Spreitzer, T. Wolfinger, J. Schenk, and R. Xu: *Metall. Mater. Trans. B.*, 2021, vol. 52B, pp. 1955–71.
20. S. Forsmo, S.-E. Forsmo, P.-O. Samskog, and B. Björkman: *Powder Technol.*, 2008, vol. 183, pp. 247–59.
21. T.K. Sandeep Kumar, N.N. Viswanathan, H.M. Ahmed, C. Andersson, and B. Björkman: *Metall. Mater. Trans. B.*, 2015, vol. 46B, pp. 635–43.
22. R. Liang, S. Yang, F. Yan, and J. He: *J. Iron Steel Res. Int.*, 2013, vol. 20, pp. 16–20.
23. D. Papanastassiou and G. Bitsianes: *Metall. Trans.*, 1973, vol. 4, pp. 487–96.
24. T.K. Sandeep Kumar, N.N. Viswanathan, H. Ahmed, A. Dahlin, C. Andersson, and B. Björkman: *Metall. Mater. Trans. B.*, 2019, vol. 50B, pp. 162–72.
25. H. Zhang, J. Fu, J. Pan, F. Zhang, and Z. Guo: *J. Wuhan Univ. Technol. Mater. Sci. Edit.*, 2018, vol. 33, pp. 1516–23.
26. H. Zhang and J. Fu: *Int. J. Miner. Metall. Mater.*, 2017, vol. 24, pp. 603–10.
27. H. Zhang, M. Lu, and J. Fu: *J. Cent. South Univ.*, 2016, vol. 23, pp. 2999–3005.
28. U. Colombo, F. Gazzarrini, G. Lanzavecchia, and G. Sironi: *Science.*, 1965, vol. 147, p. 1033.
29. U. Colombo, G. Fagherazzi, F. Gazzarrini, G. Lanzavecchia, and G. Sironi: *Nature*, 1964, p. 175.
30. E.Z. Basta: *Econ. Geol.*, 1959, vol. 54, pp. 698–719.
31. H.J. Cho, M. Tang, and P.C. Pistorius: *Metall. Mater. Trans. B.*, 2014, vol. 45B, pp. 1213–20.
32. H.J. Cho and P.C. Pistorius: *AISTech Conf.*, Association for Iron & Steel Technology (AIST), Atlanta, GA, 2012, pp. 503–11.
33. A. Sardari, E.K. Alamdari, M. Noaparast, and S.Z. Shafaei: *Int. J. Miner. Metall. Mater.*, 2017, vol. 24, pp. 486–92.
34. T.K. Sandeep Kumar, N.N. Viswanathan, H. Ahmed, A. Dahlin, C. Andersson, and B. Björkman: *Metall. Mater. Trans. B.*, 2019, vol. 50B, pp. 150–61.
35. E.R. Monazam, R.W. Breault, and R. Siriwardane: *Ind. Eng. Chem. Res.*, 2014, vol. 53, pp. 13320–28.
36. S. Song and P.C. Pistorius: *ISIJ Int.*, 2019, vol. 59, pp. 1765–9.
37. H. Zheng, J. Schenk, D. Spreitzer, T. Wolfinger, and O. Dagha-geleh: *Steel Res. Int.*, 2021, p. 2000687.
38. C.R. van Hise: *A Treatise on Metamorphism*, U.S. Government Printing Office, Washington, DC, 1904, p. 467.
39. J.W. Gruner: *Econ. Geol.*, 1926, vol. 21, pp. 375–93.
40. E. Park and O. Ostrovski: *ISIJ Int.*, 2004, vol. 44, pp. 74–81.
41. E. Park and O. Ostrovski: *ISIJ Int.*, 2004, vol. 44, pp. 999–1005.
42. D. Zhu, C. Yang, J. Pan, and X. Li: *Metall. Mater. Trans. B.*, 2016, vol. 47B, pp. 2919–30.
43. F. Pan, Q. Zhu, Z. Du, and H. Sun: *J. Iron Steel Res. Int.*, 2016, vol. 23, pp. 1160–67.
44. S.K. Bhargava, A. Garg, and N.D. Subasinghe: *Fuel.*, 2009, vol. 88, pp. 988–93.
45. E.R. Schmidt and F.H. Vermaas: *Am. Miner.*, 1955, vol. 40, pp. 422–31.
46. H. Lepp: *Am. Miner.*, 1957, vol. 42, pp. 679–81.
47. B.H. Wang: *National Ironmaking Production Technology Conf.*, Beijing, 2010, pp. 327–31.
48. C. Dupuis and G. Beaudoin: *Miner. Deposita.*, 2011, vol. 46, pp. 319–35.
49. J. Xiumin, Z. Chuguang, Q. Jianrong, L. Jubin, and L. Dechang: *Energy Fuels.*, 2001, vol. 15, pp. 1100–02.
50. J. Zhang, Q. Zhu, Z. Xie, C. Lei, and H. Li: *Metall. Mater. Trans. B.*, 2013, vol. 44B, pp. 897–905.
51. X. Fu, Y. Wang, and F. Wei: *Metall. Mater. Trans. A.*, 2010, vol. 41A, pp. 1338–48.
52. F.H. Chung: *J. Appl. Crystallogr.*, 1974, vol. 7, pp. 519–25.
53. F.H. Chung: *J. Appl. Cryst.*, 1974, vol. 7, pp. 526–31.
54. W. Wang, D. Yang, Z. Ou-Yang, R. Xu, and M. Song: *Metall. Mater. Trans. B.*, 2019, vol. 50B, pp. 678–87.
55. D. Yang, W. Wang, J. Li, R. Xu, X. Wang, and G. Wang: *Metall. Mater. Trans. B.*, 2020, vol. 51B, pp. 776–85.
56. Y. Kapelyushin, Y. Sasaki, J. Zhang, S. Jeong, and O. Ostrovski: *Metall. Mater. Trans. B.*, 2017, vol. 48B, pp. 889–99.
57. A.V. Roshchin and Vasily Roshchin: *Russ. Metall.*, 2003, pp. 1–5.
58. A. V. Roshchin and Vasily Roshchin: *Russ. Metall.*, 2003, pp. 97–102.

Publisher's Note Springer Nature remains neutral with regard to jurisdictional claims in published maps and institutional affiliations.